



# Spatial and temporal variations of summer surface temperatures of wet polygonal tundra in Siberia - implications for MODIS LST based permafrost monitoring

Moritz Langer <sup>\*</sup>, Sebastian Westermann, Julia Boike

Periglacial Section, Alfred Wegener Institute for Polar and Marine Research, Potsdam, Germany

## ARTICLE INFO

### Article history:

Received 21 October 2009

Received in revised form 16 April 2010

Accepted 17 April 2010

### Keywords:

Permafrost

Polygonal tundra

Thermal imaging

Land surface temperature

MODIS

## ABSTRACT

The surface temperature of permafrost soils in remote arctic areas is accessible by satellite land surface temperature (LST) detection. However, the spatial resolution of satellite measurements such as the MODIS LST products is limited and does not detect the heterogeneities of the wet polygonal tundra landscape where surface wetness varies over distances of several meters. This paper examines the spatial and temporal variability of summer surface temperatures of a polygonal tundra site in northern Siberia using a ground based high resolution thermal imaging system. Thermal infrared images were taken of a 1000 m<sup>2</sup> polygonal tundra area in 10 min intervals from July to September 2008. Under clear sky conditions, the individual measurements indicate temperature differences of up to 6 K between dry and wet tundra surfaces and which can exceed 12 K when dry tundra and water surfaces are compared. These differences disappear when temperature averages are considered for intervals longer than the diurnal cycle; for weekly averages the spatial temperature variability decreases below 1 K. The exception is the free water surface of a shallow polygonal pond where weekly averaged temperature differences of 2.5 K are sustained compared to the tundra surface.

The ground based thermal infrared images are upscaled to MODIS sized pixels and compared to available MODIS LST data for individual measurements and weekly averages. The comparisons show generally good agreement for the individual measurements under clear sky conditions, which exist during 20% of the studied time period. However, several erroneous measurements and large data gaps occur in the MODIS LST data during cloudy conditions, leading to biased weekly temperature averages inferred from the satellite observations. Based on these results the following recommendations are given for future permafrost temperature monitoring based on MODIS LST products: (i) high resolution surface water masks for the quality assessment in landscapes where lakes and ponds are frequent and (ii) reliable cloud cover detection in conjunction with a gap filling procedure for accurate temporal averages.

© 2010 Elsevier Inc. All rights reserved.

## 1. Introduction

The land surface temperature (LST) is the manifestation of the energy balance partition at the soil-atmosphere interface and is therefore a crucial parameter for the energy budget of permafrost environments. The sensitivity of permafrost towards degradation and the potential activation of a massive carbon source is directly associated with the energy exchange processes occurring at the soil-atmosphere interface. Especially wet tundra landscapes, where large quantities of carbon are stored in frozen organic soils, may become a massive source of green house gases under a warmer climate (Davidson & Janssens, 2006). A number of studies revealed a sustained large scale warming of the Arctic during the last decades (e.g. Comiso, 2002; Serreze et al., 2003; Stroeve et al., 2005; Overland et al., 2008; Rothrock et al., 1999), which is also reported by Comiso

(2003, 2006) using long term satellite LST measurements. The satellite observations indicate strong warming trends of LST during summer over the entire Arctic, which is essential for the summer thaw depth of permafrost soils. Hence, the monitoring of LST can be an important tool to assess the effects of climate change in the usually remote and inaccessible permafrost environments. Land surface temperatures are currently accessible by various remote sensing platforms e.g. Terra/Aqua-MODIS, Terra-ASTER, NOAA-AVHRR, Meteosat-MVIRI, ERS-ATSR and Landsat. Since they are available on a global scale with high overpass frequencies, these products have a great potential for two major applications in permafrost regions.

1. The LST provides access to atmospheric boundary layer processes in regions where climate data are sparse. Efforts have been initiated to synthesize surface-based meteorological data with satellite observations and numerical models in arctic regions (Martin & Munoz, 1997; Rigor et al., 2000). In addition, several projects in non-arctic regions, such as FIFE (Sellers et al., 1992),

<sup>\*</sup> Corresponding author.

E-mail address: [mlanger@awi.de](mailto:mlanger@awi.de) (M. Langer).

BOREAS (Sellers et al., 1995) and SEBAL (Bastiaanssen et al., 1998), examined surface energy balance models based on satellite products. A detailed overview of LST derived energy balance models is given by Friedl (2002).

- Land surface temperatures can serve as upper boundary condition in permafrost models, calculating the annual thaw depths and the thermal stability of permafrost soils. Hachem et al. (2008) introduce satellite derived land surface temperatures for permafrost detection, while essential issues such as data gaps due to cloud cover and the decoupling of soil and surface temperatures due to snow cover are addressed. A proposed scheme of satellite based permafrost modeling is given in Marchenko et al. (2009), which makes use of a MODIS LST product in combination with the analytical permafrost model GIPL-1.1. to calculate permafrost active layer dynamics for the entire Arctic.

The spatial resolution of satellite LST products typically ranges from 60 meters (Landsat) to one kilometer (MODIS). Temperature differences on smaller scales are therefore not resolved, but are nevertheless critical when they occur systematically over long time periods. In such cases, they result from sustained differences in the surface energy balance and might indicate differences in the thermal state of the subjacent permafrost, potentially triggering processes such as initial thermo karst erosion. Previous studies in non-arctic regions have outlined the effect of surface heterogeneity on satellite based energy balance detection (Brunsell & Gillies, 2003; Friedl, 1996; Hall et al., 1992; Humes et al., 1994). In particular, sub-resolution LST variations are expected to occur in highly fractionated landscapes. This is especially true for permafrost environments, such as the wet polygonal tundra, where a sharp contrast between wet and dry surface patches occurs on scales of several meters. Hence, it is desirable to elucidate the sub-resolution surface temperature variability and its impact on the accuracy of satellite permafrost monitoring schemes.

In this paper, we present summer surface temperature observations using a tower-mounted high resolution thermal imaging system at a Siberian polygonal tundra site. This surface type is characteristic for a large area of circumpolar wet tundra landscapes. At first, the spatial and temporal variability of surface temperatures obtained with the thermal camera is analyzed for the snow free period. Secondly, the MODIS L2 (collection 5) LST product (Wan, 2008) is compared to up-scaled LST data from the thermal camera and evaluated with respect to its applicability for the monitoring of permafrost active layer dynamics in wet polygonal tundra landscapes.

## 2. Site characteristics

The study was performed on Samoylov Island (72° 22' N; 126° 30' E), which represents a typical Siberian wet tundra landscape in the zone of continuous permafrost (Fig. 1a). Samoylov Island is located in the upper plain of the Lena River Delta, close to one of the main river channels (Fig. 1b). The region is characterized by an arctic continental climate. The mean annual air temperature (MAAT) at Samoylov Island is -14.7 °C and the total annual precipitation is around 250 mm, showing high inter-annual variations (Boike et al., 2008). Snow melt and Lena ice drift typically start in the beginning of June and the snow free season lasts from mid-June to mid-September. The regional permafrost reaches depths of 500–600 m (Grigoriev, 1960) and is characterized by a very low temperature of -9.2 °C at the depth of zero annual amplitude approximately 10 m beneath the surface. Samoylov Island covers an area of 4.3 km<sup>2</sup>. While the western part of the island is characterized by a recent flood plain, the eastern part consists of an elevated terrace 10–16 m a.s.l. (Fig. 1c). This terrace is characterized by wet tundra showing the typical polygonal micro-relief, which features elevation differences of 0.2 to 1.0 m. The size of the polygons typically ranges from 5 to 10 m. The depressed polygonal centers

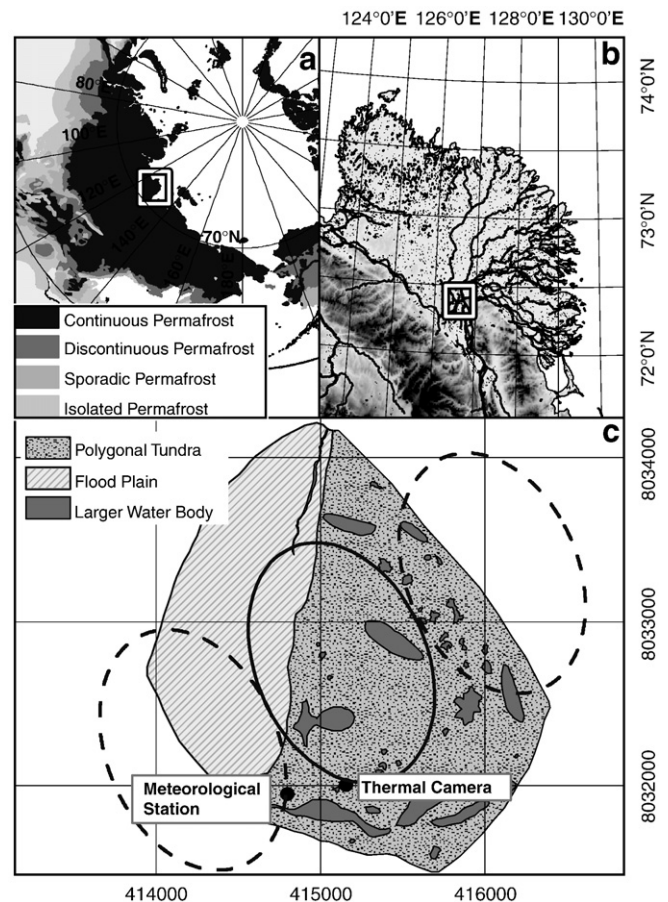


**Fig. 1.** (a) Location of the Lena River Delta in northern Siberia, the map shows the permafrost boundaries (Brown et al., 1997). (b) Location of Samoylov Island in the upper plain of the Lena River Delta close to one of the main river channels. (c) Measurement site on Samoylov, the ellipses show typical footprint areas of the MODIS scanner swath; the dashed ellipses indicate footprint areas which do not fit the 80% overlap criterion with the island (see Section 3.6).

consist of water saturated peat soils or they constitute shallow ponds. The vegetation at these wet locations is dominated by hydrophilic sedges and mosses (Kutzbach et al., 2004). The lowered centers are surrounded by elevated dry polygonal rims, which are dominated by mesophytic dwarf shrubs, forbs and mosses (Kutzbach et al., 2004; Sachs et al., 2008).

The experimental plot is located on the elevated terrace. It consists of three low center polygons and one polygonal pond surrounded by elevated dry rims (Fig. 2). Polygon (a) (Fig. 2) is characterized by a wet peaty center, which is dominated by hydrophilic mosses such as *Limprichtia revolvens*. Vascular plants are only sparsely distributed, while some mosses (pillows of *Aulacomium turgidum*) occur at the transition of the dry rim and the wet center. The vegetation of polygon (b) (Fig. 2) is characterized by sedges (*Carex aquatilis*) with a growth height of 20 cm. The sedge canopy is underlain by hydrophilic mosses. Polygon (c) (Fig. 2) is comparable in shape to polygon (a). It shows a similar vegetation cover, but is characterized by an increased number of isolated moss pillows (*Aulacomium turgidum*) occurring in the transition zone and in the polygon center. Polygon (d) (Fig. 2) contains a shallow pond, about 1.5 m deep. The edge of the pond is covered by sedges. The dry polygon rims are generally dominated by mesophilic mosses, such as *Hylocomium splendens*. Considerably more vascular plants occur at the dry locations. The elevation differences of the investigated polygons vary between 0.2 to 0.5 m. The water level is mostly located directly underneath the surface of the wet polygonal centers, resulting in a patchy structure of puddles and moss agglomerations. During the

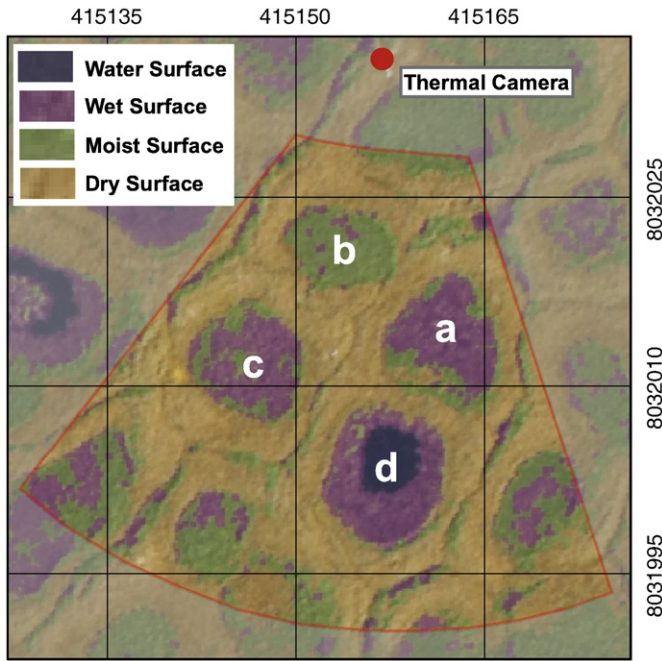


**Fig. 2.** Field of view of the thermal imaging system (about 1000 m<sup>2</sup>). Surface classification based on aerial images taken on 08/15/2008 (projection: UTM 52N WGS84). The considered polygonal structures (a) and (c) are typical low center wet polygons with moss dominated centers, while polygon (b) is dominated by sedges and polygon (d) is filled by a shallow pond with a free water surface.

observation period the water level decreased about 5 cm, while occasional rain events temporarily raised the water table.

### 3. Methods

#### 3.1. Experimental setup

The surface temperature measurements were conducted using a tower mounted high resolution thermal camera (VARIOCAM HR, Infratec GmbH, Dresden, Germany). The VARIOCAM thermal imaging system consists of an uncooled microbolometer detector with a resolution of 384 × 288 pixels. The spectral sensitivity ranges from 7.5 to 14 μm and the imaging system is equipped with a 12 mm wide angle lens. After passing the lens, the incoming thermal radiation is focused on the microbolometer array, which is thermally stabilized at the ambient temperature. The absorbed thermal radiation induces temperature changes at the bolometer elements that are measurable due to changes in electrical resistance. A detailed description of the principle of uncooled microbolometers is given by [Dereniak and Boreman \(1996\)](#). The sensitivity of thermal radiation detectors is expressed by the Noise Equivalent Temperature Difference (NETD), which is smaller than 30 mK for the applied imaging system. The camera is mounted on an 11 m tower and is oriented south with an off-nadir angle of 55°. This inclination is consistent with the recommended angles for radiative temperature measurements of vegetated surfaces ([Huband & Monteith, 1986](#); [Vining & Blad, 1992](#)). The setup facilitates continuous surface temperature measurements of an area of about 1000 m<sup>2</sup> ([Fig. 2](#)). The measurements were conducted from end of July until end of September 2008. With a measurement interval of 10 minutes, a database of more than 7000 thermograms could be obtained.

Ancillary meteorological data such as radiation, precipitation and soil temperatures are obtained in the immediate vicinity of the measurement plot ([Fig. 1](#)). Soil temperatures are detected by three thermistor profiles (107-L, Campbell Scientific Incorporated, Logan, Utah, USA) and the precipitation is measured by an automatic rain gauge (ARG100, Ingenieursbureau Wittich & Visser, Netherlands). The

radiation balance is detected by a four component radiation sensor (CNR1, Kipp & Zonen, Delft, Netherlands), calibrated according to WMO standards. In this study, the radiation directed towards the surface is defined as positive. During the measurement period high resolution visible (VIS) and near infrared (NIR) orthorectified aerial images of Samoylov Island were obtained (cp. [Scheritz et al., 2008](#)). To obtain a land cover classification, the aerial photographs are further processed by a supervised maximum likelihood classification. We distinguish water bodies, wet, moist and dry surfaces ([Fig. 2](#)). The entire area of the island consists of 15% free water surfaces, 26% wet areas, 32% dry surfaces and 27% moist areas.

#### 3.2. Theory

According to Planck's law the emitted spectral intensity of a black body  $B(T, \lambda)$  is related to its temperature  $T$ ,

$$B(T, \lambda) = \frac{2hc^2}{\lambda^5} \frac{1}{e^{\frac{hc}{\lambda kT}} - 1}, \quad (1)$$

where  $\lambda$  is the wavelength,  $h$  the Planck constant,  $k$  the Boltzmann constant and  $c$  the speed of light. Following the terminology of [Norman and Becker \(1995\)](#), surface temperatures obtained from radiance measurements under the black body assumption are called brightness temperatures  $T_B$ . The thermal camera is calibrated to deliver brightness temperatures, from which we can evaluate the corresponding radiation  $R_s(T_B)$  received at the thermal imaging system in the 7.5 to 14 μm spectral window

$$R_s(T_B) = \int_{7.5\mu m}^{14\mu m} B(T_B, \lambda) d\lambda. \quad (2)$$

Natural surfaces usually do not feature black body characteristics. The spectral intensity of thermal radiation  $B_n$  leaving a natural surface is modified due to the spectral emission characteristics of the surface. Using Kirchhoff's law we obtain:

$$B_n(T_0, \theta, \phi, \lambda) = \epsilon(\theta, \phi, \lambda) B(T_0, \lambda) + [1 - \epsilon(\theta, \phi, \lambda)] B_{sky}(\theta', \phi', \lambda), \quad (3)$$

where  $T_0$  denotes the surface temperature,  $\epsilon$  the spectral directional emissivity and  $B_{sky}$  the spectral intensity of the sky radiation. Note that the emissivity and sky radiation induce an angular dependence from the zenith angle  $\theta$  and azimuth angle  $\phi$  with the corresponding opposite angles  $(\theta', \phi')$ . The thermal radiation leaving the surface is affected by absorption and emitted thermal radiation originating from the traversed air column, which can be accounted for by a transmission coefficient  $\tau$ , depending on the path length  $s$  and an additional radiation source  $B_{air}$ , respectively. Using Eq. (3) we obtain

$$R_s(T_0, \theta, \phi, s) = \int_{7.5\mu m}^{14\mu m} \tau(s, \lambda) [\epsilon(\theta, \phi, \lambda) B(T_0, \lambda) + [1 - \epsilon(\theta, \phi, \lambda)] B_{sky}(\theta', \phi', \lambda)] + B_{air}(s, \lambda) d\lambda. \quad (4)$$

For our analysis, the following assumptions are used:

- 1) The absorption and emission of thermal radiation in the traversed air column is mostly due to water vapor. In our case, the maximum path length through the air column is 35 meters, and the maximum absolute air-water content measured during the study period is 14 gm<sup>-3</sup> (LI-7500 gas analyzer located 300 m from the study site). The combined effect of absorption and emission of radiation in the air is evaluated for the measured temperature and humidity range using the 'libRadtran' software package based on



the 'uvspec' radiative transfer model (Mayer & Kylling, 2005). The results indicate a maximum modification of 0.4% of the thermal radiation received at the thermal camera. This results in a maximum error  $\Delta T_{\text{absorb}}$  of about 0.3 K in surface temperature, which we include in our error analysis (Fig. 3).

- 2) We assume an emissivity  $\bar{\epsilon}$ , which is independent of wavelength and view angle. The resulting error ranges from 0 to 1.5 K and is included in the error calculation (see Section 3.3 and Fig. 3).
- 3) The thermal sky radiation is assumed to be isotropic. The downwelling sky radiation measured by the pyrgeometer  $R_{\text{sky}}$  (spectral range from 5 to 42  $\mu\text{m}$ ) is used to estimate the thermal radiation emitted by the sky over the entire spectral range. The ambient sky temperature  $T_{\text{sky}}$  is calculated assuming black-body behavior using Stefan-Boltzman's law:

$$R_{\text{sky}} = \sigma T_{\text{sky}}^4, \quad (5)$$

where  $\sigma$  denotes the Stephan-Boltzmann constant. With  $T_{\text{sky}}$ , we can evaluate  $B_{\text{sky}}(\lambda)$  similar to Eq. (1)

The black body assumption is a good approximation for overcast conditions, which prevail during a large part of the study period (see Section 4.1). An additional error may occur for clear sky conditions, where the spectral distribution of the sky radiation is different from a black body.

As a result of these assumptions, Eq. (4) can be simplified to:

$$R_s(T_0, T_{\text{sky}}, \bar{\epsilon}) = \bar{\epsilon} \int_{7.5\mu\text{m}}^{14\mu\text{m}} B(T_0, \lambda) d\lambda + (1 - \bar{\epsilon}) \int_{7.5\mu\text{m}}^{14\mu\text{m}} B(T_{\text{sky}}, \lambda) d\lambda, \quad (6)$$

where  $\bar{\epsilon}$  is the effective emissivity as described in Eq. (7) in the following section. Using Eqs. (2) and (6), the surface temperature  $T_0$  can be evaluated via a numerical equation solver (MATLAB). Note that the solution is unambiguous, since the integral over Planck's function from 7.5 to 14  $\mu\text{m}$  is monotonous with respect to temperature in the relevant temperature range.

### 3.3. Land surface emissivity determination

The land surface emissivity (LSE) is a crucial parameter for radiative measurement of surface temperatures (see Section 3.2). We determine emissivities using the land cover classification based on aerial images (Fig. 2). We distinguish water and dry vegetation as two basic classes, for which we use spectrally resolved emissivities provided by the MODIS USCB emissivity library (Wan & Zhang, 1999). The corresponding effective emissivity values  $\bar{\epsilon}$  in the 7.5 to 14  $\mu\text{m}$  window are then calculated as:

$$\bar{\epsilon} = \frac{\int_{7.5\mu\text{m}}^{14\mu\text{m}} \epsilon(\lambda) B(T_0, \lambda) d\lambda}{\int_{7.5\mu\text{m}}^{14\mu\text{m}} B(T_0, \lambda) d\lambda} \quad (7)$$

This yields emissivities of 0.985 for water and 0.964 for dry vegetation. Note that the temperature dependence of  $\bar{\epsilon}$  is negligible in the considered temperature range from  $-10^\circ\text{C}$  to  $40^\circ\text{C}$  (around 0.0005). The emissivities of the wet and moist tundra classes are set by estimating the fractions of water and dry vegetation in each class from field observations, with 50% water and 50% dry vegetation for wet tundra and 25% water and 75% dry vegetation for moist tundra, respectively. This results in emissivity values of 0.975 for wet tundra and 0.969 for moist tundra. Our values are in good agreement with published emissivity values for similar surfaces, which range from

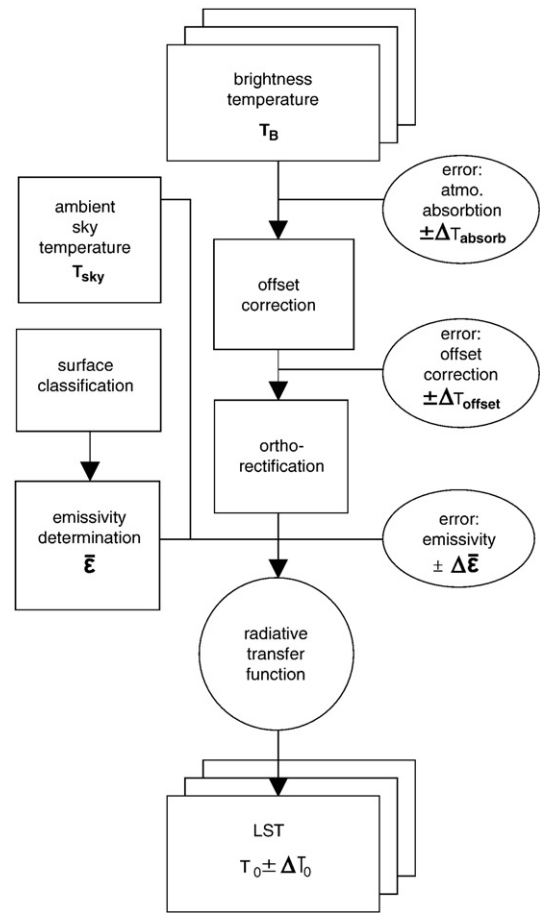


Fig. 3. Work flow of the thermal camera data processing from brightness to land surface temperatures (LST) including error margins. Total errors  $\Delta T_0$  are based on Gaussian error propagation.

0.96 for dry vegetation to 0.99 for water (Rees, 1993; Salisbury & D'Aria, 1992; Snyder et al., 1998).

A potential view angle dependence of the emissivity, which may become substantial under extreme off-nadir angles, induces uncertainty in the obtained surface temperature  $T_0$  (Becker et al., 1985; Labed & Stoll, 1991; Snyder et al., 1997, 1998). Norman and Becker (1995) report a slight decrease of the emissivity of about 0.01 for forest canopies at off-nadir angles of  $75^\circ$ . Snyder and Wan (1998) compare modeled and measured directional emissivity values. They report a maximum emissivity decreases of 0.046 for savanna, 0.042 for dry soils and 0.01 for water. Following these reported angular emissivity variations, we assume a maximum error  $\Delta\epsilon$  of 0.04 for all used emissivities. For the emissivity values calculated above, this error margin also accounts for possible wrongly classified points. Furthermore, all measurements under off-nadir angles of more than  $75^\circ$  are excluded from our analysis. The induced error on temperature due to the uncertainty of the emissivities is included in the error calculation (Fig. 3). This temperature error is small when the ambient sky temperature approaches the surface temperature (see Eq. (6)), which is the case for overcast conditions, which frequently occur at the study site.

### 3.4. Offset correction

The thermal imaging system shows a vignetting-like decrease in the measured temperatures from the center towards the edges, which becomes obvious during overcast conditions, where surface temperatures show almost no spatial variations. The temperature offset is circular, with a maximum value of 0.8 K at the corners of the image. Due to the shape and the consistent occurrence in thermograms with little

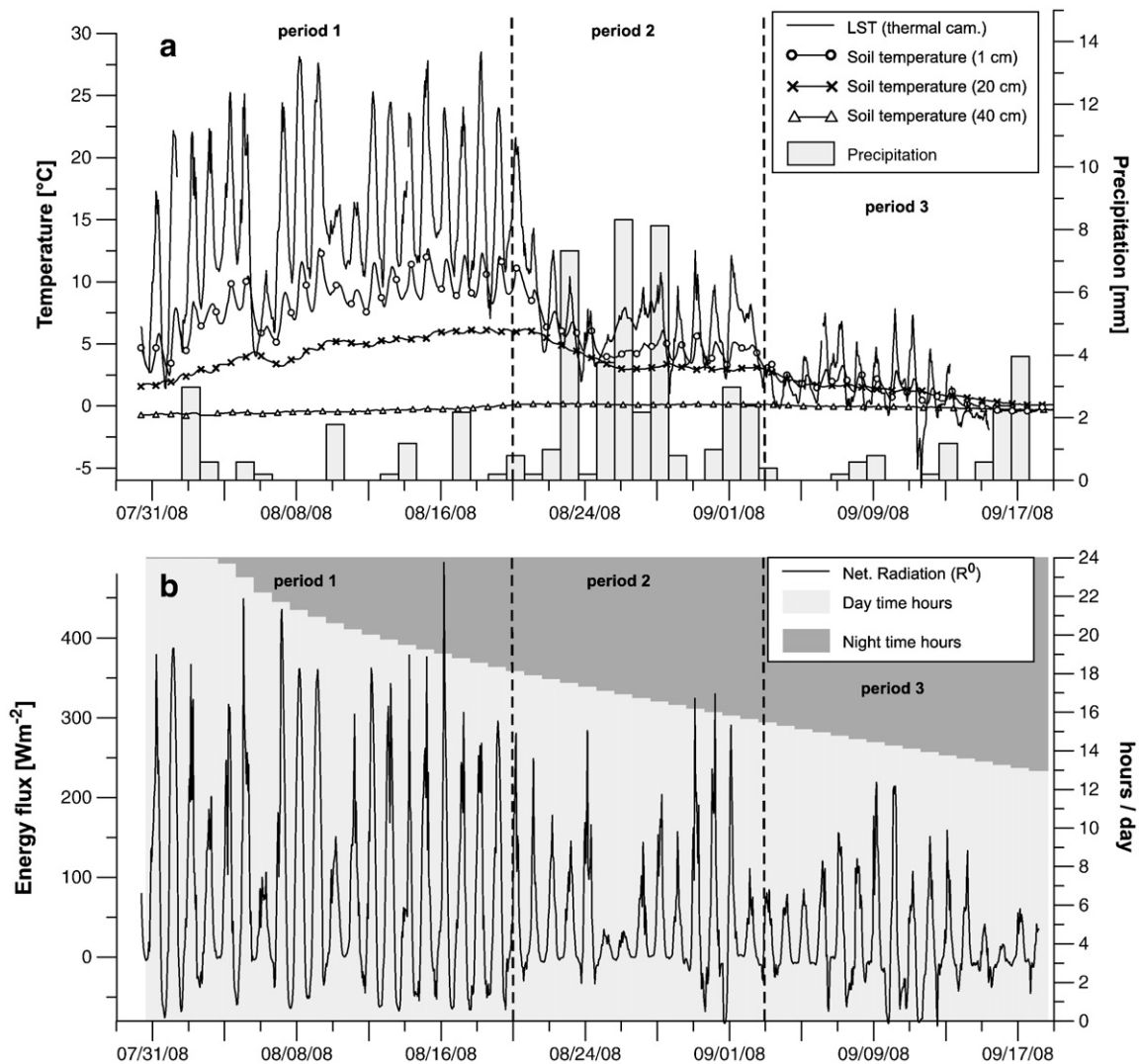


**Fig. 4.** (a) Seasonal variations of surface temperature, precipitation and soil temperatures in 1 cm, 20 cm and 40 cm depth during the observation period in 2008. (b) Seasonal variations of net radiation and day time hours during the observation period. The observation period is divided in three distinct intervals of synoptic conditions.

temperature variation, we can assume the temperature offset to be a systematic error present within the entire data set. To correct for the offset on the edges of the thermograms, a two-dimensional second-order polynomial with rotational symmetry is fitted to more than 400 scenes with approximately homogeneous surface temperatures. From this, an average correction matrix is extracted, which is used for correction of the entire data set. The variability within the 95% confidence limits of the fitted polynomial coefficients is used to provide an error estimate on the temperatures due to the correction procedure. The maximum errors occurring at the edges of the thermograms are on the order of 0.2 K, which we assume to be an additional temperature uncertainty  $\Delta T_{\text{offset}}$  induced by the offset correction procedure. The temperature uncertainty is included in the error analysis (Fig. 3).

### 3.5. Geometrical correction

To obtain spatially resolved surface temperature measurements with equal pixel sizes it is necessary to orthorectify the thermograms. This geometrical correction is accomplished by a transfer function, which accounts for the internal camera geometry and the external orientation parameters (Slama et al., 1980). The internal camera parameters include the sensor and pixel size, the focal length and two radial lens distortion parameters. The external camera orientation is

defined by the position and the view angles of the imaging system. While the sensor and pixel size are provided by the manufacturer of the thermal imaging system, the remaining parameters can be calculated from a sufficiently large set of image and corresponding ground control points (Slama et al., 1980). This set of points is obtained by relating distinct features in the thermograms to structures of an orthorectified aerial image where the coordinates are known. Hereby, the small elevation differences of the micro-relief are neglected and the images are projected on a plane. The resulting horizontal displacement error is smaller than 1.0 m.

### 3.6. Satellite data set

We evaluate the performance of the MODIS L2 (collection 5) LST products (MOD11L2.5 and MYD11L2.5) obtained by the satellites Terra and Aqua at the study site. The satellite data are obtained from the National Aeronautics and Space Administration Land Processes Distributed Active Archive Center (Wan, 2008). These products contain processed surface temperatures using the generalized split window approach (Wan & Dozier, 1996). The LST retrieval is based on the bands 31 and 32 covering a spectral range from 10.8 to 12.3  $\mu\text{m}$ . The required surface emissivities in the bands 31 and 32 are estimated from land cover types. The accuracy of the MODIS LST (collection 5) product is

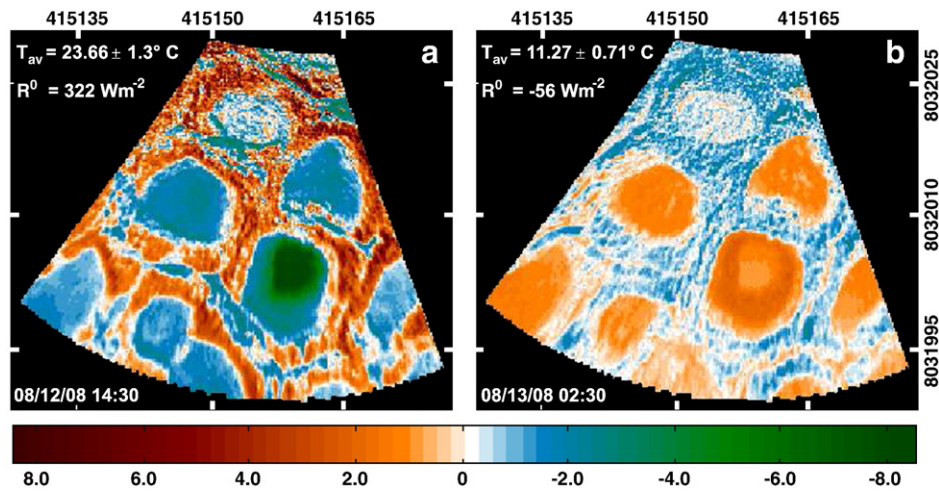


**Fig. 5.** Surface temperature differences in Kelvin from the average scene temperature  $T_{av}$  for (a) day and (b) night time situation under clear sky conditions. The examples illustrate the highest sun position at 08/12/08 (a) and the lowest sun position at 08/13/08 (b) reached 2.5 hours after local noon and midnight (times in the diagrams are local times). The average scene temperature  $T_{av}$  is defined as the average over the entire thermogram with the average error margins  $\pm \Delta T_{av}$ .  $R^0$  denotes the net radiation.

specified to be in the range of 1 K (Wan, 2008). The applied L2 product provides the unprojected swath data format (Wan, 2009), from which the footprint area of the MODIS pixels and the exact acquisition time can be calculated. In the case of Samoylov Island, which only covers an area of about 4.3 km<sup>2</sup>, it is crucial to control the footprint area to avoid influences of the surrounding Lena River. For the footprint analysis, we use the additional MODIS geolocation products MOD03 and MYD03 featuring an accuracy of 50 m at nadir angles (Wolfe et al., 2002). The field of view of each sensor pixel is assumed to be circular (Nishihama et al., 1997). Based on the geolocation products and the internal sensor parameters such as focal length and sensor size, the measurement spot is projected on the earth surface, resulting in an elliptically shaped footprint of a sensor pixel. Depending on view angle 0–55° and distance, the measurement spot varies in shape and size (see Fig. 1c for example). The region of interest within the satellite scene is selected to represent the surface of the island (compare Section 2). Mixed pixels containing fractions of the Lena River of more than 20% are discarded (see Fig. 1c). Due to the polar orbits of the satellites Terra and Aqua, a high overpass frequency is obtained in polar regions. Hence, up to 18 satellite scenes are potentially available per day at the investigation site. During the observation period from end of July until end of September 2008, a total of 1077 MODIS granules is used.

## 4. Results

### 4.1. General synoptic conditions

The measurement period extends from the end of the polar day season until equinox in fall (08/01 – 09/17) (Fig. 4). It can be divided into three distinct periods, each characterized by different weather conditions (Fig. 4a). The first period (08/01 – 08/19) is characterized by large positive values of net radiation, high surface temperatures and a warming of the subjacent soil. The second period (08/20 – 09/02) is dominated by cloudy conditions with frequent rain events and low values of net radiation. This results in generally low surface temperatures, which are associated with decreasing soil temperatures. Due to lower sun angles and increased night hours, the third period (09/03 – 09/17) is characterized by steadily decreasing surface and soil temperatures. However, clear sky conditions frequently occur especially in the middle of period (3), but are interrupted by sporadic rain events. Towards the end of the third period the surface temperatures sometimes fall below the freezing point, which results in occasional ice layer formation at the polygonal pond.

### 4.2. Short term spatial variability

A typical day and night time surface temperature situation under clear sky conditions during period (1) is displayed Fig. 5. These examples, in which the net radiation  $R^0$  amounts to 330 W m<sup>-2</sup> during the day and -50 W m<sup>-2</sup> during the night, illustrate the surface temperature variations as they occur under strong radiative forcing. The orthorectified thermograms show the difference of each pixel from the average temperature over the entire field of view, which we define as the average scene temperature  $T_{av}$ . During day time a sharp temperature contrast exists between the dry polygonal rims and the wet centers (Fig. 5a). The observed deviations from the average scene temperature are 4 to 6 K for the dry rims, -2 to -1 K for the wet centers, and about -6 K for the pond. These spatial surface temperature differences are clearly outside the total error margins  $\Delta T_0$ , which are 1.0 K for the scene average. The largest error is found at the dry rims, which could be as large as 1.7 K, while the lowest temperature uncertainty of 0.6 K occurs at the free water surface. Compared to the other wet locations, polygon (b) shows a higher surface temperature with no difference to the scene average. The increased temperature of polygon (b) is probably explained by the high fraction of vertically oriented dry vegetation elements seen by the inclined imaging system, since polygon (b) is dominated by sedges (compare Section 2). During night time the temperature situation reverses (Fig. 5b) and the temperature differences between the wet and dry surfaces are less pronounced. Now the dry locations are about 1 K colder than the scene average, including the sedge dominated center, which again is in contrast to the other wet locations. The other wet locations remain 1.0 to 1.5 K warmer than the average scene temperature, which reflects the large heat storage capacity of the water saturated soils. During the night the polygonal pond remains the warmest surface, with a temperature of 2 K above the scene average. Even so, the spatial temperature differences are less pronounced, they are still larger than the maximum temperature error of 0.7 K found at the dry rims. The different temporal temperature behavior of wet and dry surfaces is mostly a result of distinctly different diurnal temperature amplitudes. For the given example, the diurnal temperature amplitude of the dry rims is twice as large as at the one of the wet polygonal centers.

Under cloudy conditions or low sun angles as typical for periods (2) and (3), the temperature contrast between wet and dry locations is less pronounced. This is illustrated in Fig. 6, which shows the relationship between the net radiation  $R^0$  and the temperature differences between the scene averages  $T_{av}$  and the single surface classes  $T_0$ , such as wet, moist, dry and water surfaces (compare

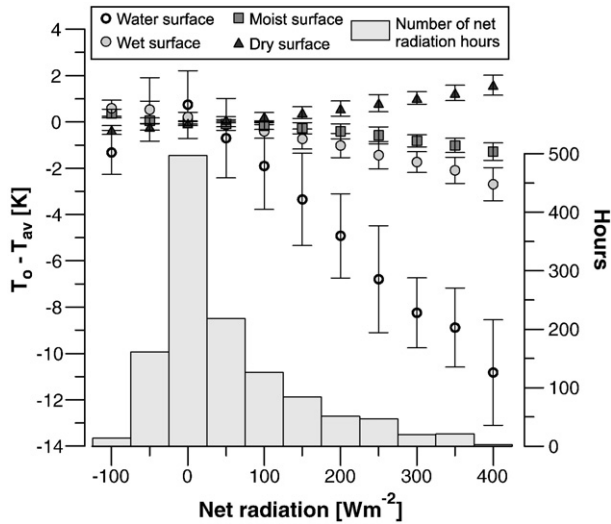


**Fig. 6.** Surface temperature differences from the scene average ( $T_0 - T_{av}$ ) versus net radiation, as found for hourly averages of the different surface classes. The binning of the net radiation is set to  $50 \text{ W m}^{-2}$ , the standard deviations within the radiation classes are indicated by error bars. The histogram shows the distribution of net radiation hours as they occur during the observation period.

Section 3.1). For high values of net radiation, significant differences between surface temperatures are observed, while these differences vanish for zero net radiation. The net radiation can hence be identified as the main factor for the formation of spatial temperature variations. A significant spread remains (see Fig. 6), which can be explained by the influence of other components of the surface energy budget, such as sensible, latent and ground heat fluxes. For positive values of net radiation, the temperatures of dry surfaces are increased compared to the wet and moist surfaces. The most pronounced temperature difference to the average scene temperature is found for the free water surface of the polygonal pond. This behavior reverses for a negative net radiation budget, with exception of the free water surfaces. The very low surface temperatures of the water body during the periods of highly negative net radiation ( $-100 \text{ W m}^{-2}$ ) lead to significant negative temperature difference to the scene average. This behavior could be associated with occasional ice cover formation during these times. As shown in Fig. 6, the measurement period is dominated by net radiation values between  $-50$  and  $50 \text{ W m}^{-2}$ , while conditions of high radiative forcing are comparatively rare. Hence, the temperature distribution is rather homogeneous for a large part of the study period. Situations with pronounced surface temperature differences, as shown in Fig. 5, are not characteristic for the observation period.

#### 4.3. Long term spatial variability

Since the diurnal temperature cycle is damped rapidly in deeper soil layers, only the average surface temperature trend is reflected in the development of the ground temperatures. Fig. 4a displays surface temperatures and corresponding soil temperatures at depths of 1, 20 and 40 cm, which show that the diurnal temperature cycle is damped out below 20 cm depth. In contrast to the short term diurnal temperature variations, the long term surface temperature signal determined by the three synoptic periods propagates down to the thaw front. Since significant temperature changes usually occur on time scales longer than one week, weekly averages of LST are appropriate time intervals to resolve the general soil thermal dynamics during the observation period. The spatial variability of the surface temperatures can only lead to temperature differences in deeper soil layers, if the surface temperature differences are persistent in averages over such longer periods.

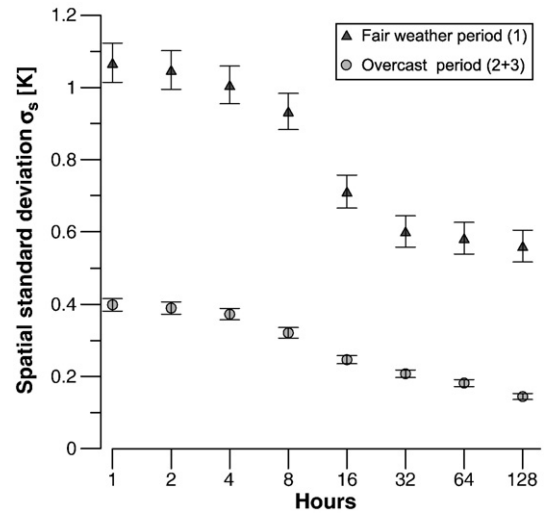


**Fig. 7.** Reduction of the mean spatial standard deviation due to increasing temporal averaging intervals for periods dominated by fair weather and overcast conditions. The standard deviations over the scenes are a good approximation for the spatial surface temperature variability. In both cases, the initial variability is reduced by a factor of two after averaging over more than 128 hours. Note that the time scale is logarithmic.

To investigate the general effect of temporal averaging on the spatial temperature variability, the spatial surface temperature variability is evaluated for a number of different averaging intervals (Fig. 7). We only illustrate averaging intervals up to 128 hours, since no significant changes occur for longer intervals. We divide the entire measurement period in predominately fair weather (period 1) and overcast (period 2 + 3) conditions. Averaged time series of thermograms are constructed from these sub-periods, featuring averaging intervals between 0 and 128 hours. From the obtained aggregated time series we evaluate the average spatial standard deviations ( $\sigma_s$ ), which give us a measure of the spatial surface temperature variability during the sub-periods. It can be seen in Fig. 7, that the averaging procedure significantly reduces the spatial variability in surface temperature. The spatial standard deviations of the fair weather condition decrease from about 1.1 K to 0.6 K for averaging intervals of 1 and 128 hours. Compared to the fair weather conditions, the spatial temperature variability is generally lower for the overcast periods, which is a result of decreased radiative forcing under cloudy conditions (see Section 4.2). During the overcast periods, the average spatial standard deviation is 0.4 K for 1 hour averages, which again decreases by a factor of two for intervals of 128 hours. The most effective reduction of temperature variability occurs when the averaging interval covers the time span from solar noon to solar midnight, so that the diurnal amplitude averages out. Since the displayed standard deviations are based on averaging intervals starting at solar noon, the most pronounced reduction of spatial temperature variability occurs at the 12 hour interval for both synoptic situations (see Fig. 7).

In any case, the spatial variability of surface temperature is strongly reduced for averaging periods of one week, which determine the general temperature development of the subadjacent soil column. Three examples of weekly averaged thermograms, each representative for one period as shown in Fig. 4, are displayed in Fig. 8a–c. The temporal variations within the weekly averages are indicated as images of standard deviation (Fig. 8d–f). Sustained differences in average surface temperatures are only observed during period (1). With a total temperature difference of about 1 K between dry and wet surfaces, they are small and in the range of the error  $\Delta T_0$ , which amounts to 0.8 K for the dry rims and to 0.6 K for the scene average. The only considerable temperature difference to scene average of  $-2.2 \text{ K}$  is generated at the free water surface of the pond, where



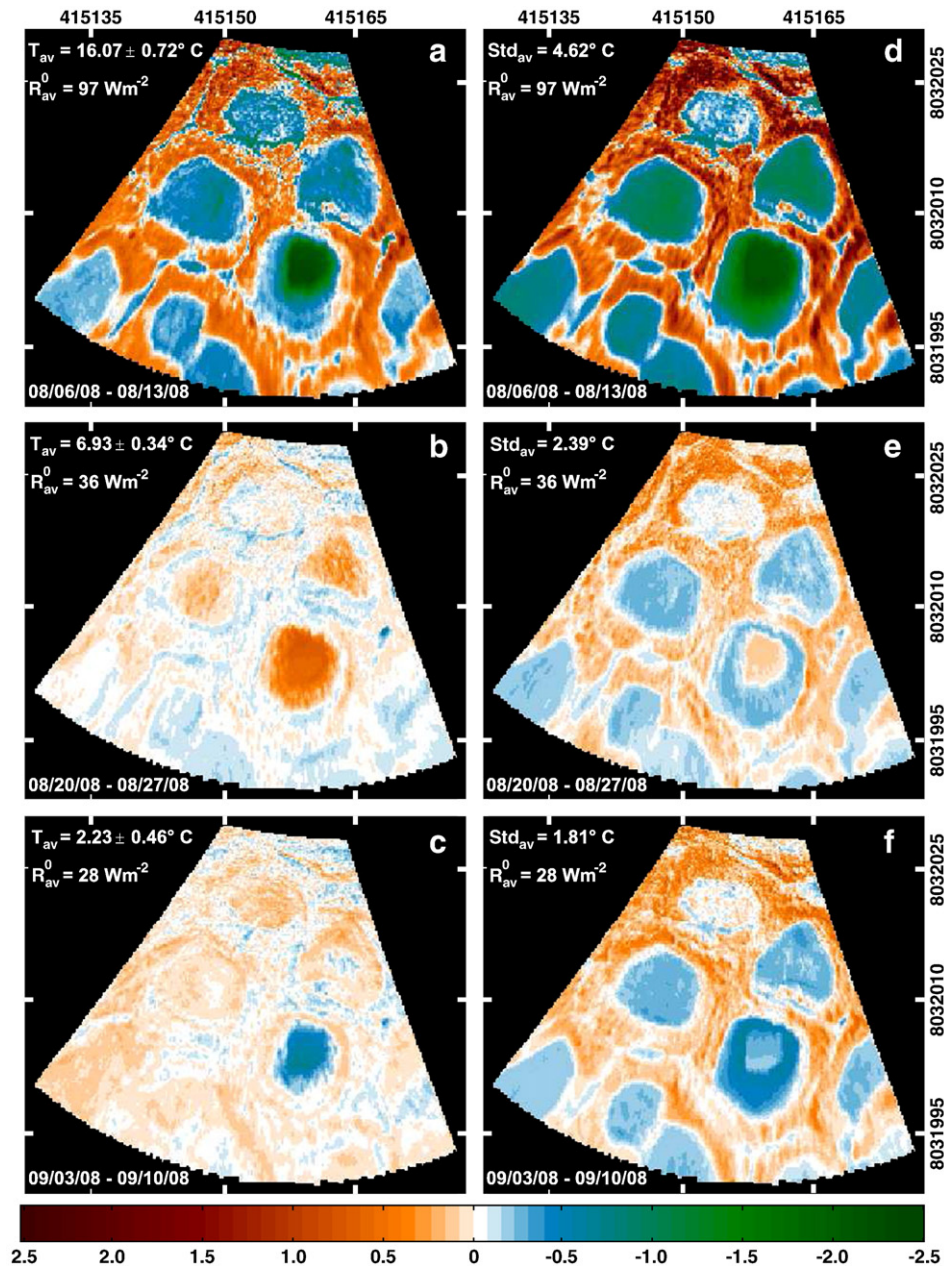


**Fig. 8.** Weekly averages of surface temperature variations in Kelvin in the periods 1 (a), 2 (b), and 3 (c) (similar to Fig. 5). Surface temperature differences steadily decrease over the course of the observation period. The same is found for the corresponding standard deviations  $Std_{av}$  (d, e, f), but they show a higher spatial contrast.  $R_{av}^0$  denotes the average net radiation. Note that the color bar is valid for all thermograms.

the temperature uncertainty is found to be 0.5 K (see Fig. 8a). The pronounced diurnal cycle, as described in Section 4.2, results in high values of the standard deviation (Fig. 8d). A sharp contrast exists between the standard deviations of the wet and dry surfaces, which reflects their differences in the diurnal temperature amplitude. The average values of the period (2) show only insignificant spatial differences in surface temperature (Fig. 8b). The pond is now warmer than the other surfaces, which is probably due to the large heat storage of the water body. The predominately cloudy conditions with low values of net radiation during period (2) lead to reduced standard deviations (Fig. 8e), which indicate the reduced diurnal temperature amplitude compared to period (1). Furthermore, strong temperature differences occur relatively rarely in period (2), which is reflected in the reduced spatial contrast of the standard deviation. During the third period (Fig. 8c), almost no temperature differences are observed between the wet polygonal centers and the dry rims. The average

surface temperature is close to the freezing point and occasional ice cover formation on the pond has been observed towards the end of period (3). This ice cover possibly explains the pond surface temperatures well below the freezing point, but the effect is not fully understood since only few data are available at the very end of the observation period. Compared to the previous period, the standard deviation does not show significant differences (Fig. 8f). With exception of the free water surface, the observed spatial temperature differences during period (1) and period (2) are not significant because they fall within the margin of error, which is in the order of 0.4 K for both periods.

In the weekly averages only the pond shows a surface temperature, which is distinctly different from the other surfaces. The temperature differences between wet and dry tundra surfaces are reduced to an insignificant level within the weekly averages. These results demonstrate that almost no long-term spatial temperature



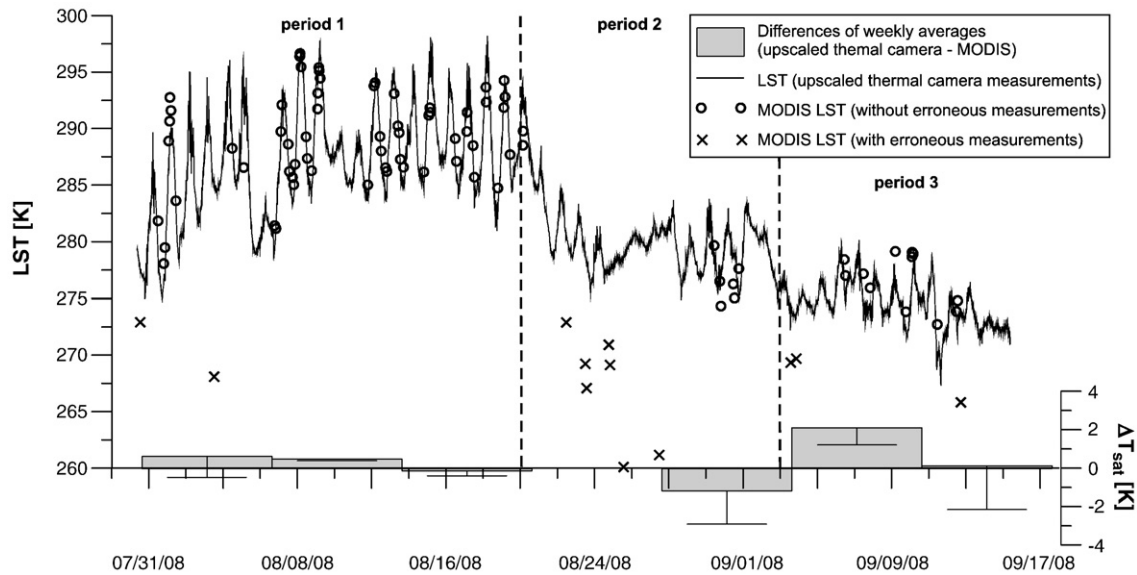


**Fig. 9.** Land surface temperature (LST), as observed by the thermal camera and MODIS sensor (erroneous data are marked). The differences between the weekly averages of the thermal camera and the satellite data  $\Delta T_{sat}$  are low for the first weeks, where the data density is high. The satellite LST averages are strongly biased, where the data density is sparse and the erroneous measurements induce additional temperature offsets (error bars).

differences occur at the polygonal tundra surface. Hence, sustained surface temperature differences due to the heterogeneous surface characteristics of the polygonal tundra can be excluded as a potential source of spatial variability soil temperatures in deeper layers.

#### 4.4. MODIS surface temperature observations

We compare the MODIS MOD11L2.5 and MYD11L2.5 LST products with the surface temperature measurements of the terrestrial thermal imaging system (Fig. 9). The local surface temperature measurements of the thermal camera are upscaled by weighting the fractions of 26% wet, 27% moist, 32% dry and 15% water areas, as obtained by the land cover classification over the entire island (see Section 3.1). The surface classes are uniformly distributed over the island, so that all valid MODIS footprint areas represent the surface composition of the island. The average measurement density during the entire observation period is two measurements per day. The strong reduction of the potential 18 overpasses per day not only originates from cloud cover, but also from footprint areas, which do not match the 80% overlap criterion (see Section 3.6 and Fig. 1). Especially satellite measurements under oblique angles produce footprint areas, which are much larger than the optimum footprint area of 1 km<sup>2</sup> and can exceed the total surface area of the island. In general, the satellite data are in good agreement with the measurements of the thermal camera (Fig. 9). Nevertheless, on few occasions the satellite measurements deviate strongly from the terrestrial observations, most likely caused by incorrect cloud cover evaluation. These measurements are found to be 5 to 15 K colder than the temperatures inferred from the thermal camera, which indicates that cloud top temperatures are measured rather than land surface temperatures. For this reason, these data values are classified as erroneous measurements (Fig. 9). In addition to the cloud cover mask, the MODIS product provides quality flags, which might help to exclude cloud affected data values. The flags indicate that almost the entire data set is affected by nearby clouds. A general exclusion of these data would result in a 90% reduction of the data set over the entire period, which would be an unnecessary limitation, since most data values are found to be reasonable compared to terrestrial observations (Fig. 9). In period (1) the average measurement density of three successful satellite observations per day is high due to prevailing clear sky conditions. Only two erroneous measurements are observed at the beginning of the period.

During period (2), which is dominated by overcast conditions, few successful satellite observations are obtained, exclusively during short periods of clear sky conditions. The achieved average measurement density is 0.6 per day. Most of the data received during this period must be considered as erroneous. Period (3) is characterized by frequent clear sky conditions, resulting in a number of successful satellite measurements without erroneous data. The average measurement density during period (3) is one per day.

We now compare the weekly averages of the available satellite data with the true averages obtained by the thermal camera. The weekly surface temperature values are based on step wise averaging, using previous averages with hourly and daily intervals, in order to avoid the over representation of clumped satellite data. The differences between the weekly averages of the upscaled thermal camera data and the MODIS product with and without erroneous data are illustrated in Fig. 9. The erroneous measurements of the satellite data set lead to a strong additional bias of the average values, especially when the data density is sparse. The following evaluation is conducted under the assumption that a reliable cloud cover mask is provided in order to separate the effect of erroneous data from the effect of the unequally spaced satellite time series on the average temperature values. In period (1), the satellite averages are in very good agreement with the terrestrial observations due to the high data density. During the beginning of period (2) average values can not be calculated, since no measurements other than erroneous observations are available. At the end of period (2) satellite data are predominately available during the night and the late afternoon, which results in an underestimated average surface temperature. During period (3) satellite data are frequently obtained near local noontime, which leads to an overestimated average value. Hence, the averaging procedure fails under conditions with low measurement density and a systematic over representation of certain daytimes.

#### 5. Discussion

On time scales longer than the diurnal cycle, the results of this study show that the surface temperature variations, except for free water surfaces, average out. Hence, our results imply that permafrost temperatures in the polygonal tundra are not affected by spatial surface temperature differences due to heterogeneities of surface soil moisture. Sustained differences in surface temperature occur at free

water bodies, such as the examined polygonal pond, which shows a surface temperature offset of 2.5 K in the weekly average during period (1). The observed surface temperature differences between the pond and the tundra surface are most likely the result of a distinctly different energy partition at free water bodies induced by efficient energy storage due to convective heat transport and absorption of solar radiation in the water column or at the ground. The effect of energy balance differences of lakes on regional arctic climates has been shown in measurements by Rouse et al. (2005) and simulations by Krinner (2003), Gutowski et al. (2007) and Krinner and Boike (in press), who demonstrate the significantly different energy exchange processes at high latitude lakes compared to the surrounding soil surface. It can be expected that larger fractions of water bodies within the spatial averaging area induce significant temperature offsets.

Assuming that the results of this study can be transferred to other arctic wet tundra regions, unresolved spatial surface temperature heterogeneities are not a limitation for permafrost monitoring schemes based on remote sensing LST measurements. Temporal averages of satellite LST measurements are valid for the covered surface area, even so landscape heterogeneities are not resolved by the sensor, as long as the fraction of free water surfaces is small. This has been implicitly assumed in the permafrost monitoring schemes by Hachem et al. (2008) and Marchenko et al. (2009). Hence, LST products such as MODIS L2 with a spatial resolution of about 1 km<sup>2</sup> are applicable for permafrost monitoring schemes. However, such schemes require accurate temporal LST averages, which are necessarily based upon accurate measurements in appropriate temporal density. Due to these requirements three major problems are identified for the development of satellite based permafrost monitoring schemes:

- 1) The temporal resolution of the satellite time series is strongly affected by cloud cover, which leads to clustered time series, where averaging is problematic. Hence, reliable gap filling methods must be developed. Possible gap filling procedures are demonstrated by Hachem et al. (2008), other approaches might be based on reanalysis products.
- 2) The existing cloud cover detection of satellite products such as MODIS must be improved, since unidentifiable measurement errors result in strongly biased average temperatures, especially when data are sparse. In the present state, this problem would make reliable gap filling methods more difficult or even impossible.
- 3) For satellite pixels with a high fraction of free water surfaces, a biased temperature record for the land area is likely. Further work on the effect of water bodies, such as polygonal ponds and thermokarst lakes, on the larger-scale surface temperature and energy balance is desirable for the implementation of LST products in future schemes of permafrost monitoring in wet tundra landscapes.

Although the results show that spatial temperature differences vanish on longer time scales, they are important for atmospheric energy exchange processes acting on much shorter time scales. The observed short term spatial surface temperature differences are mainly controlled by the by net radiation. Under clear sky conditions and strong radiative forcing, the temperature differences between wet and dry locations can be on the order of 4 to 6 K and exceed 12 K between open water bodies and dry surfaces. The temperature variations indicate distinctly different surface energy budgets, which can be caused by differences in albedo, energy storage in the ground, aerodynamic resistance or resistance to evapotranspiration. The surface temperature differences at wet and dry locations lead to distinctly different sources of sensible heat fluxes in immediate vicinity of each other. Furthermore, the differences in surface soil moisture most likely result in different evapotranspiration rates and thus latent heat fluxes. Due to the small distance between the sensible

and latent heat flux sources, energy reallocation processes are possible, which could affect the energy balance on a larger scale (e.g. Guo & Schuepp, 1994; Mahrt et al., 1994; Neumann & Marsh, 1998). A better understanding of the relation between these small-scale processes and the larger-scale boundary layer dynamics, which are the result of accumulated local energy exchange processes, would enhance the process knowledge of the landscape specific climate dynamics in wet tundra regions.

## 6. Summary and Conclusion

The spatial and temporal characteristics of summer surface temperatures of a heterogeneous polygonal tundra landscape are investigated using ground based high resolution thermal infrared measurements. The measurements are used for ground-truthing a MODIS LST product. The following conclusions are drawn with respect to future satellite permafrost monitoring schemes:

- The spatial surface temperature variations at the wet polygonal tundra greatly reduce for averaging periods longer than the diurnal cycle. This has strong implications for satellite based permafrost monitoring schemes, since the validity of surface temperature averages is not affected by unresolved landscape heterogeneities, except for free water bodies.
- Free water bodies show sustained differences in surface temperature to the remaining tundra surface. Hence, high resolution land-water masks are essential for the interpretation of satellite LST products, since unresolved water bodies can bias the satellite observations, if a high fraction occurs in the satellite footprint area.
- The success rate of MODIS LST data acquisition is limited due to a frequent cloud cover, which is typical for arctic regions. Reliable surface temperature averages therefore require the development of gap filling procedures. Furthermore, the satellite data are biased by occasional erroneous measurements, which are caused by an incorrect cloud cover mask. This limitation should be overcome to enhance the data quality of the LST product.

Satellite based LST measurements bear great potential as a basic input parameter for a monitoring scheme of the thermal state of permafrost soils. However, continued effort will be required to overcome the mentioned limitations, if such monitoring schemes are intended to be applied on large scales.

## Acknowledgments

We thank the following for their assistance in the field, technical support and for discussion: Niko Bornemann, Maren Grüber, Sina Muster and Konstanze Piel. Thanks to the logistical support of the Russian-German research station on Samoylov that made this study possible. We gratefully acknowledge the financial support by the Helmholtz Association (HGF) through a grant (VH-NG 203) awarded to Julia Boike.

## References

- Bastiaanssen, W., Menenti, M., Feddes, R., & Holtslag, A. (1998). A remote sensing surface energy balance algorithm for land (SEBAL). 1. Formulation. *Journal of Hydrology*, 212, 198–212.
- Becker, F., Ramanantsoahena, P., & Stoll, M. (1985). Angular variation of the bidirectional reflectance of bare soils in the thermal infrared band. *Applied Optics*, 24(3), 365–375.
- Boike, J., Wille, C., & Abnizova, A. (2008). Climatology and summer energy and water balance of polygonal tundra in the Lena River Delta, Siberia. *Journal of Geophysical Research-Biogeosciences*, 113(G3), G03025.
- Brown, J., Ferrians Jr., O., Heginbottom, J., Melnikov, E. (1997). Circum-Arctic map of permafrost and ground-ice conditions. US Geological Survey Circum-Pacific Map.
- Brunsell, N., & Gillies, R. (2003). Scale issues in land-atmosphere interactions: implications for remote sensing of the surface energy balance. *Agricultural and Forest Meteorology*, 117(3–4), 203–221.
- Comiso, J. (2002). A rapidly declining perennial sea ice cover in the Arctic. *Geophysical Research Letters*, 29(20), 1956.

- Comiso, J. (2003). Warming trends in the Arctic from clear sky satellite observations. *Journal of Climate*, 16(21), 3498–3510.
- Comiso, J. (2006). Arctic warming signals from satellite observations. *Weather*, 61(3), 349–351.
- Davidson, E., & Janssens, I. (2006). Temperature sensitivity of soil carbon decomposition and feedbacks to climate change. *Nature*, 440(7081), 165–173.
- Dereniak, E., & Boreman, G. (1996). *Infrared detectors and systems*. Wiley-Interscience.
- Friedl, M. (1996). Relationships among remotely sensed data, surface energy balance, and area-averaged fluxes over partially vegetated land surfaces. *Journal of Applied Meteorology*, 35(11), 2091–2103.
- Friedl, M. (2002). Forward and inverse modeling of land surface energy balance using surface temperature measurements. *Remote Sensing of Environment*, 79(2), 344–354.
- Grigoriev, N. (1960). The temperature of permafrost in the Lena delta basin – deposit conditions and properties of the permafrost in Yakutia. Yakutsk, Ch. 2, pp. 97–101, in Russian.
- Guo, Y., & Schuepp, P. (1994). An Analysis of the Effect of Local Heat Advection on Evaporation over Wet and Dry Surface Strips. *Journal of Climate*, 7(5), 641–652.
- Gutowski, W., Jr., Wei, H., Vörösmarty, C., & Fekete, B. (2007). Influence of Arctic wetlands on Arctic atmospheric circulation. *Journal of Climate*, 20(16), 4243–4254.
- Hachem, S., Allard, M., & Duguay, C. (2008). A new permafrost map of Quebec-Labrador derived from near-surface temperature data of the moderate resolution imaging spectroradiometer (MODIS). *Proceedings, NICOP, Vol. I*. (pp. 591–596).
- Hall, F., Huemmrich, K., Goetz, S., Sellers, P., & Nickeson, J. (1992). Satellite remote sensing of surface energy balance: success, failures, and unresolved issues in FIFE. *Journal of Geophysical Research*, 97(D17), 19061–19089.
- Huband, N., & Monteith, J. (1986). Radiative surface temperature and energy balance of a wheat canopy. *Boundary-Layer Meteorology*, 36(1), 1–17.
- Humes, K., Kustas, W., Moran, M., Nichols, W., & Weltz, M. (1994). Variability of emissivity and surface temperature over a sparsely vegetated surface. *Water Resources Research*, 30(5), 1299–1310.
- Krinner, G. (2003). Impact of lakes and wetlands on boreal climate. *Journal of Geophysical Research-Atmospheres*, 108(D16), 4520.
- Krinner, G., & Boike, J. (2010). A study of the large-scale climatic effects of a possible disappearance of highlatitude inland water surfaces during the 21st century. *Boreal Environment Research*, 15, 203–217.
- Kutzbach, L., Wagner, D., & Pfeiffer, E. (2004). Effect of microrelief and vegetation on methane emission from wet polygonal tundra, Lena Delta, Northern Siberia. *Biogeochemistry*, 69(3), 341–362.
- Labeled, J., & Stoll, M. (1991). Angular variation of land surface spectral emissivity in the thermal infrared: laboratory investigations on bare soils. *International Journal of Remote Sensing*, 12(11), 2299–2310.
- Mahrt, L., MacPherson, J., & Desjardins, R. (1994). Observations of fluxes over heterogeneous surfaces. *Boundary-Layer Meteorology*, 67(4), 345–367.
- Marchenko, S., Hachem, S., Romanovsky, V., & Duguay, C. (2009). Permafrost and Active Layer Modeling in the Northern Eurasia using MODIS Land Surface Temperature as an input data. *Geophysical Research Abstracts*, 11, EGU2009–EGU11077.
- Martin, S., & Munoz, E. (1997). Properties of the Arctic 2-meter air temperature field for 1979 to the present derived from a new gridded dataset. *Journal of Climate*, 10(6), 1428–1440.
- Mayer, B., & Kylling, A. (2005). Technical note: The libRadtran software package for radiative transfer calculations—description and examples of use. *Atmospheric Chemistry and Physics*, 5, 1855–1877.
- Neumann, N., & Marsh, P. (1998). Local advection of sensible heat in the snowmelt landscape of Arctic tundra. *Hydrological Processes*, 12(10), 1547–1560.
- Nishihama, M., Wolfe, R., Solomon, D., Patt, F., Blanchette, J., Fleig, A., Masuoka, E. (1997). MODIS level 1A Earth location: Algorithm theoretical basis document version 3.0. SDST-092, MODIS Science Data Support Team.
- Norman, J., & Becker, F. (1995). Terminology in thermal infrared remote sensing of natural surfaces. *Agricultural and Forest Meteorology*, 77(3–4), 153–166.
- Overland, J., Wang, M., & Salo, S. (2008). The recent Arctic warm period. *Tellus A*, 60(4), 589–597.
- Rees, W. (1993). Infrared emissivity of Arctic winter snow. *International Journal of Remote Sensing*, 14(16), 3069–3073.
- Rigor, I., Colony, R., & Martin, S. (2000). Variations in surface air temperature observations in the Arctic, 1979–97. *Journal of Climate*, 13(5), 896–914.
- Rothrock, D., Yu, Y., & Maykut, G. (1999). Thinning of the Arctic sea-ice cover. *Geophysical Research Letters*, 26(23), 3469–3472.
- Rouse, W., Oswald, C., Binyamin, J., Spence, C., Schertzer, W., Blanken, P., et al. (2005). The role of northern lakes in a regional energy balance. *Journal of Hydrometeorology*, 6(3), 291–305.
- Sachs, T., Wille, C., Boike, J., & Kutzbach, L. (2008). Environmental controls on ecosystem-scale CH<sub>4</sub> emission from polygonal tundra in the Lena River Delta, Siberia. *Journal of Geophysical Research. G. Biogeosciences*, 113, G00A03.
- Salisbury, J., & D'Aria, D. (1992). Emissivity of terrestrial materials in the 8–14 microns atmospheric window. *Remote Sensing of Environment*, 42(2), 83–106.
- Scheritz, M., Dietrich, R., Scheller, S., Schneider, W., & Boike, J. (2008). Digital Elevation Model of Polygonal Patterned Ground on Samoylov Island, Siberia, Using Small-Format Aerial Photography. *Proceedings, NICOP, Vol. II*. (pp. 1589–1594).
- Sellers, P., Hall, F., Asrar, G., Strebel, D., & Murphy, R. (1992). An overview of the first international satellite land surface climatology project (ISLSCP) field experiment (FIFE). *Journal of Geophysical Research*, 97(D17), 18345–18371.
- Sellers, P., Hall, F., Ranson, K., Margolis, H., Kelly, B., Baldocchi, D., et al. (1995). The Boreal Ecosystem–Atmosphere Study (BOREAS): an overview and early results from the 1994 field year. *Bulletin of the American Meteorological Society*, 76(9), 1549–1577.
- Serreze, M., Maslanik, J., Scambos, T., Fetterer, F., Stroeve, J., Knowles, K., et al. (2003). A record minimum arctic sea ice extent and area in 2002. *Geophysical Research Letters*, 30(3), 1110.
- Slama, C., Theurer, C., & Henriksen, S. (1980). *Manual of photogrammetry*. Virginia: American Society of Photogrammetry Falls Church.
- Snyder, W., & Wan, Z. (1998). BRDF models to predict spectral reflectance and emissivity in the thermal infrared. *IEEE Transactions on Geoscience and Remote Sensing*, 36(1), 214–225.
- Snyder, W., Wan, Z., Zhang, Y., & Feng, Y. (1997). Thermal infrared (3–14 micron) bidirectional reflectance measurements of sands and soils. *Remote Sensing of Environment*, 60(1), 101–109.
- Snyder, W., Wan, Z., Zhang, Y., & Feng, Y. (1998). Classification-based emissivity for land surface temperature measurement from space. *International Journal of Remote Sensing*, 19(14), 2753–2774.
- Stroeve, J., Serreze, M., Fetterer, F., Arbetter, T., Meier, W., Maslanik, J., et al. (2005). Tracking the Arctic's shrinking ice cover: another extreme minimum in 2004. *Geophysical Research Letters*, 32(4), L04501.
- Vining, R., & Blad, B. (1992). Estimation of sensible heat flux from remotely sensed canopy temperatures. *Journal of Geophysical Research*, 97(D17), 18951–18954.
- Wan, Z. (2008). New refinements and validation of the MODIS land-surface temperature/emissivity products. *Remote Sensing of Environment*, 112(1), 59–74.
- Wan, Z. (2009). MODIS land surface temperature products users' guide. <http://www.icess.ucsb.edu/modis/LstUsrGuide/usrguide.html>.
- Wan, Z., & Dozier, J. (1996). A generalized split-window algorithm for retrieving land-surface temperature from space. *IEEE Transactions on Geoscience and Remote Sensing*, 34(4), 892–905.
- Wan, Z., Zhang, T., 1999. MODIS UCSB Emissivity Library: <http://www.icess.ucsb.edu/modis/EMIS/html/em.html>.
- Wolfe, R., Nishihama, M., Fleig, A., Kuyper, J., Roy, D., Storey, J., et al. (2002). Achieving sub-pixel geolocation accuracy in support of MODIS land science. *Remote Sensing of Environment*, 83(1–2), 31–49.